

A statistical-based approach for acoustic tomography of the atmosphere

Soheil Kolouri and Mahmood R. Azimi-Sadjadi^{a)}

Electrical and Computer Engineering Department, Colorado State University, Fort Collins, Colorado 80523-1373

Astrid Ziemann

Institute of Hydrology and Meteorology, Technische Universität Dresden, Dresden, 01062, Germany

(Received 7 August 2012; revised 29 October 2013; accepted 1 November 2013)

Acoustic travel-time tomography of the atmosphere is a nonlinear inverse problem which attempts to reconstruct temperature and wind velocity fields in the atmospheric surface layer using the dependence of sound speed on temperature and wind velocity fields along the propagation path. This paper presents a statistical-based acoustic travel-time tomography algorithm based on dual state-parameter unscented Kalman filter (UKF) which is capable of reconstructing and tracking, in time, temperature, and wind velocity fields (state variables) as well as the dynamic model parameters within a specified investigation area. An adaptive 3-D spatial-temporal autoregressive model is used to capture the state evolution in the UKF. The observations used in the dual state-parameter UKF process consist of the acoustic time of arrivals measured for every pair of transmitter/receiver nodes deployed in the investigation area. The proposed method is then applied to the data set collected at the Meteorological Observatory Lindenberg, Germany, as part of the STINHO experiment, and the reconstruction results are presented.

© 2014 Acoustical Society of America. [<http://dx.doi.org/10.1121/1.4835875>]

PACS number(s): 43.28.We, 43.28.Vd, 43.28.Lv, 43.25.Ts [VEO]

Pages: 104–114

I. INTRODUCTION

Acoustic tomography is a method of remotely reconstructing the internal structure of an object by radiating acoustic signals through the object and studying its interactions with the signals. Owing to their non-intrusive nature, acoustic tomography methods have been used excessively in medical, non-destructive testing and measurement, oceanographic, and atmospheric arenas.

Knowledge about temperature and wind velocity fields is of great importance in atmospheric surface layer studies. Acoustic tomography of the atmosphere allows one to reconstruct temperature and wind velocity fields in the atmospheric surface layer using the dependence of sound speed on temperature and wind velocity fields along the propagation path. Atmospheric acoustic tomography methods^{1–8} are very useful due to their ability to provide spatially and temporally resolved fields for model evaluation and their scalability property. Moreover, using acoustic tomography is highly beneficial, as it uses a small number of acoustic sensors to reconstruct the temperature and wind velocity fields with high spatial resolution. Algorithms dealing with acoustic tomography of the atmosphere, use the acoustic travel time measurements collected from several acoustic sensors (transmitters and receivers) mostly located on the boundary layer of the investigation field. The travel time for each propagation path corresponds with the line integral of a nonlinear function of temperature and wind velocity fields over the propagation path.

An inverse acoustic travel-time tomography problem is inherently an under-determined and ill-posed problem due to the fact that it attempts to reconstruct the continuous temperature and wind velocity fields from finite travel time measurements. Solving such problem is in general difficult, owing to its ill-posed and highly nonlinear nature. However, several tomographic algorithms have been introduced^{1–6,8} in different disciplines to solve the acoustic tomography problem. These tomographic algorithms are categorized into three main branches as statistical-based algorithms,^{1,5,6,8} algebraic-based algorithms,^{3,4,9–11} and those which use sparse reconstruction framework.¹⁰

Wilson and Thomson¹ applied a statistical-based acoustic tomography algorithm referred to as stochastic inversion (SI), to reconstruct the temperature and wind velocity fields. Later, Vecherin and co-workers^{5,6} extended this algorithm by developing the time-dependent stochastic inversion (TDSI), which uses several travel time observations to generate the estimates of the fields. These methods use a first-order linear approximation of the group velocity of the sound wave along the propagation path and solve the linearized problem using a discrete, noncausal Wiener filter.¹² The SI assumes that turbulence is statistically homogeneous in space, while TDSI assumes that fluctuations are homogeneous in space and also stationary in time. However, extreme temporal change of atmospheric patterns may render a non-adaptive filter such as Wiener filter inefficient. More recently, a statistical-based method⁸ was introduced which casts this acoustic tomography problem as a state estimation and hence employs unscented Kalman filter (UKF) to reconstruct the temperature and wind velocity fields. This method can provide: (a) nonlinear acoustic travel time tomography

^{a)}Author to whom correspondence should be addressed. Electronic mail: azimi@engr.colostate.edu

under certain measurement conditions, (b) reconstruction without the need for reciprocal measurements as in Refs. 3, 4, and 13, (c) adaptive behavior for tracking the fields in time, and (d) computational efficiency for possible on-line implementation. We acknowledge that the relative errors of linearization in case of low wind conditions is negligible and using UKF would be exorbitant. However, the proposed approach provides a general framework which works under both strong and weak wind conditions.⁸

Algebraic-based acoustic tomography algorithms, such as multiplicative algebraic reconstruction technique¹⁴ and simultaneously iterative reconstruction technique,^{3,13} employ reciprocal sensors and reformulate the nonlinear problem into two linear problems using the reciprocal measurements. Then, they reconstruct temperature and wind velocity fields separately using a gradient-based iterative ℓ_2 minimization algorithm. Generally speaking, the algebraic-based methods^{3,13,14} are conceptually simpler than the statistical-based tomography algorithms. However, comparing to the statistical-based methods, algebraic-based methods are shown to lack accuracy for undetermined problems.⁶

Algorithms using sparse reconstruction framework assume that the temperature and wind velocity fields can be represented as a linear combination of some kernel functions (e.g., set of different bases) where most of the coefficients are zero. In other words, they assume that the fields have sparse representation with respect to some known bases in space or frequency domains. An acoustic tomography algorithm is developed in Ref. 10, based on sparse reconstruction framework. The algorithm in Ref. 10 is developed for a numerical experiment in which the wind velocity is set to zero, meaning that it is assumed that the travel time measurements are only dependent on the temperature field.

The focus of this paper is on improving the acoustic tomography method introduced in Ref. 8. The investigation area is discretized into several grids in which the temperature and wind velocity fields are assumed to be constant. The problem is then represented as an adaptive dual state-parameter estimation framework. Using this adaptive dual state-parameter estimation process one is able to account for the temporal changes (short-term or longterm) inherent in the temperature and wind velocity fields. The state and model parameter vectors are formed of the temperature and wind velocity fields in all grids and the unknown parameters of a 3-D spatial-temporal autoregressive (AR) model used to capture the state evolution dynamics, respectively. The observation vector consists of the noisy acoustic travel time measurements for every pair of transmitter/receivers nodes. Dual UKF is then used to estimate the state and model parameters simultaneously at every snapshot.¹⁵⁻¹⁷ The initial states are chosen to be the temperature and wind velocity spatial mean fields calculated from the noisy travel time measurements and the initial model parameters are chosen so that the initial state evolution model is a random walk. The proposed method is then applied to the travel time data set acquired as part of the STINHO experiment¹⁸ to reconstruct temperature and wind velocity fields and it is shown that the reconstruction results are indeed promising.

This paper is organized as follows. Section II reviews the acoustic tomography inverse problem formulation. The

proposed inverse acoustic tomography method is described in detail in Sec. III. The proposed method is applied to the STINHO data set and the reconstruction results are provided and discussed in Sec. IV. Finally, the conclusions are presented in Sec. V.

II. PROBLEM FORMULATION

A. Review of acoustic propagation formulation

Taking into account the effect of wind velocity, the magnitude of group velocity of a sound wave propagating along a specific path is given by

$$c_{\text{ray}}(\mathbf{r}, t) = \mathbf{s} \cdot (c(\mathbf{r}, t)\mathbf{n} + \mathbf{v}(\mathbf{r}, t)), \quad (1)$$

where $\mathbf{r} = x\mathbf{e}_x + y\mathbf{e}_y$ is the position vector of a point in the investigation area with \mathbf{e}_x and \mathbf{e}_y being the unit vectors of a 2D-Cartesian coordinate system, t represents time, \mathbf{s} and \mathbf{n} are, respectively, unit vectors along the propagation path and normal to wavefront, $\mathbf{v}(\mathbf{r}, t)$ is the wind velocity vector, and c is the temperature-dependent adiabatic sound speed.^{1,5,6}

For a setup in which the maximum length of the path between the acoustic transmitters and receivers are a few hundreds of meters and assuming that the vertical temperature gradient in the atmospheric surface layer is not large, one can use the straight-ray model for acoustic propagation.¹ Straight-ray model is commonly used throughout the literature and states that \mathbf{s} and \mathbf{n} are in the same direction and hence $\mathbf{s} \cdot \mathbf{n} \approx 1$. However, in presence of (a) large temperature or wind velocity gradients or (b) high wind speed, using the straight-ray model leads to non-unique solutions of the wind velocity field. Jovanovic¹⁹ suggested using time-difference of arrivals among tripoles of transmitters and receivers to estimate the angles of departure/arrival, namely, \mathbf{n}_T and \mathbf{n}_R of the sound wave. A linear fit can then be employed to produce the estimate of $\mathbf{n}(\mathbf{r}, t)$ between these points given the path. Ray-tracing can be employed [refer to Eq. (3.33) in Ref. 20] in this bent-ray model to estimate $\mathbf{s}(\mathbf{r}, t)$ along the path based upon prior estimates of the temperature and wind fields, i.e.,

$$\mathbf{s}(\mathbf{r}, t) = \frac{\mathbf{n}c(\mathbf{r}, t-1) + \mathbf{v}(\mathbf{r}, t-1)}{\|\mathbf{n}c(\mathbf{r}, t-1) + \mathbf{v}(\mathbf{r}, t-1)\|}, \quad (2)$$

where one can initially start with straight rays as the first approximations. As new wind and temperature field reconstructions become available the accuracy of ray-tracing improves. In Sec. III, we shall see how this bent-ray model can be incorporated into the proposed UKF-based reconstruction method. It must be noted that in Sec. IV due to low wind conditions during the data collection process and lack of angle of arrival measurements we assumed $\mathbf{s} \cdot \mathbf{n} = 1$. We acknowledge that this assumption ($\mathbf{s} \cdot \mathbf{n} = 1$) enables a linear representation of the process. However, our goal here is to illustrate how one would use the proposed approach for a general nonlinear problem.

Once $\mathbf{s}(\mathbf{r}, t)$ and $\mathbf{n}(\mathbf{r}, t)$ are estimated along each path, Eq. (1) can be rewritten as

$$c_{\text{ray}}(\mathbf{r}, t) = \zeta(\mathbf{r}, t)c(\mathbf{r}, t) + \mathbf{s}(\mathbf{r}, t) \cdot \mathbf{v}(\mathbf{r}, t), \quad (3)$$

where $\xi(\mathbf{r}, t) = \mathbf{s}(\mathbf{r}, t) \cdot \mathbf{n}(\mathbf{r}, t)$. Given the group velocity of the sound wave propagating along the n th path, the acoustic travel time for this path is given by

$$\tau_n(t) = \int_{L_n} \frac{dl_n}{c_{\text{ray}}(\mathbf{r}, t)} = \int_{L_n} \frac{dl_n}{\xi_n(\mathbf{r}, t)c(\mathbf{r}, t) + \mathbf{s}_n(\mathbf{r}, t) \cdot \mathbf{v}(\mathbf{r}, t)}, \quad (4)$$

where the integration is along the n th propagation path with length L_n and $\mathbf{s}_n(\mathbf{r}, t)$ is the unit vector in the direction of the wave propagation at location \mathbf{r} and time snapshot t .

Discretizing the investigation area into $I \times J$ grids and assuming that the temperature and wind velocity are constant in each grid, Eq. (4) can be discretized as

$$\tau_n(t) = \sum_{i=1}^I \sum_{j=1}^J \frac{d_n(i, j)}{\xi_n([i, j], t)c([i, j], t) + \mathbf{s}_n([i, j], t) \cdot \mathbf{v}([i, j], t)}, \quad (5)$$

where $d_n(i, j)$ is the distance n th propagation path travels in the (i, j) th cell, $c([i, j], t)$ and $\mathbf{v}([i, j], t)$ are the adiabatic sound speed and the wind velocity vector in the (i, j) th grid at time t , respectively. Here we represent the wind velocity vector in terms of two decoupled variables, namely, the magnitude and angle (instead of coupled vertical and horizontal wind velocity components), i.e.,

$$\mathbf{v}([i, j], t) = \alpha([i, j], t)\cos(\theta[i, j], t)\mathbf{e}_x + \alpha([i, j], t)\sin(\theta[i, j], t)\mathbf{e}_y, \quad (6)$$

where $\alpha(\mathbf{r}, t)$ and $\theta(\mathbf{r}, t)$ are magnitude and direction of the wind velocity in the (i, j) th grid and at time t , respectively. Note that polar coordinates are used for the wind velocity due to the need for decoupled state variables in the UKF. Additionally, using this type of state definition provides useful insight about the spatio-temporal properties of each component individually. Using Eq. (6), the term $\mathbf{s}_n(\mathbf{r}, t) \cdot \mathbf{v}([i, j], t)$ in Eq. (5) can be written as

$$\mathbf{s}_n \cdot \mathbf{v}([i, j], t) = \alpha([i, j], t)\cos(\theta[i, j], t)\cos(\phi_n[i, j], t) + \alpha([i, j], t)\sin(\theta[i, j], t)\sin(\phi_n[i, j], t), \quad (7)$$

where $\phi_n([i, j], t)$ is the angle of the n th propagation path with \mathbf{e}_x in the $[i, j]$ th grid.

B. State-space model

As pointed out before, in order to discretize the problem, the deployment field is divided into non-overlapping $I \times J$ grids as shown in Fig. 1. The fields are assumed to be constant in each grid cell. The sound speed, wind velocity amplitude and wind velocity angle at all grid cells are then arranged to form the $L = 3IJ$ -dimensional state vector as

$$\mathbf{x}_t = [\mathbf{c}^T(t), \boldsymbol{\alpha}^T(t), \boldsymbol{\theta}^T(t)]^T, \quad (8)$$

where $\mathbf{c}(t) = [c([1,1], t), c([1,2], t), \dots, c([I, J], t)]^T$ is the column vector of the sound speed at every grid, and similarly

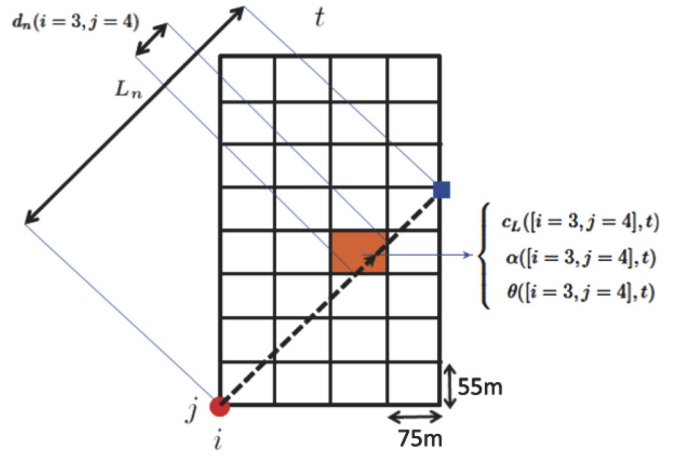


FIG. 1. (Color online) Discretization process of the investigation area into several grids and the parameters used in each grid to represent the acoustic travel time for every propagation path.

for $\alpha(t)$ and $\theta(t)$. The observation vector, \mathbf{y}_t , on the other hand, consists of all travel time measurements for all acoustic propagation paths. That is,

$$\mathbf{y}_t = [\tau_1(t), \dots, \tau_N(t)]^T, \quad (9)$$

where $\tau_i(t)$ is the travel time for the i th path at snapshot t .

A 3-D spatial-temporal AR model is used to capture the state evolution in two consecutive snapshots. The support region of this 3-D AR model is illustrated in Fig. 2 for the sound speed field at time t . This 3-D AR model for modeling the dynamics of the sound speed field is given by

$$\begin{aligned} \mathbf{c}([i, j], t) = & \rho_0^c \mathbf{c}([i, j], t-1) + \rho_1^c (\mathbf{c}([i+1, j], t-1) \\ & + \mathbf{c}([i-1, j], t-1) \\ & + \mathbf{c}([i, j+1], t-1) + \mathbf{c}([i, j-1], t-1)) \\ & + \rho_2^c (\mathbf{c}([i+1, j+1], t-1) \\ & + \mathbf{c}([i+1, j-1], t-1) \\ & + \mathbf{c}([i-1, j+1], t-1) \\ & + \mathbf{c}([i-1, j-1], t-1)) + u_c([i, j], t), \end{aligned} \quad (10)$$

where ρ_0^c , ρ_1^c , and ρ_2^c are the AR model coefficients of the sound speed field, and $u_c([i, j], t)$ is the driving process for this

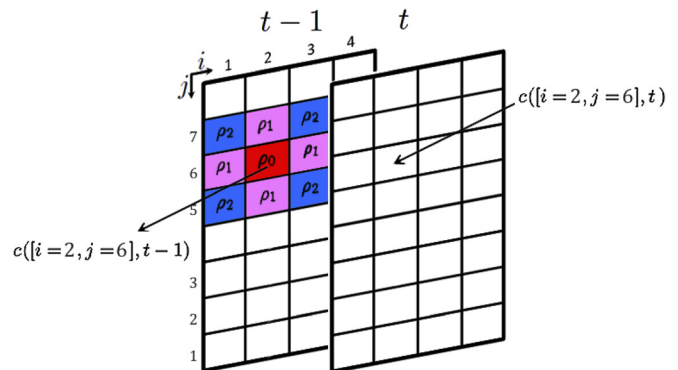


FIG. 2. (Color online) Support region of a first order spatial-temporal 3-D AR model shows how each state at grid (i, j) and time t is related to the associated states in the region of support at time $(t-1)$.

model. For each field the adjacent neighbors at time $t - 1$ are used as the support region for each grid at time t . Note that around the boundaries the support region of a cell is reduced to its neighbors in the investigation area. For the cells around the boundaries, the neighbors that are outside the investigation area are set to zero. Similar 3-D AR models are used for the wind velocity amplitude and angle fields.

The AR model for the sound speed can be rewritten in state equation vector form as

$$A^{(c)}(\boldsymbol{\rho}_t^c) \triangleq \begin{bmatrix} B(\boldsymbol{\rho}_t^c) & C(\boldsymbol{\rho}_t^c) & \mathbf{0} & \mathbf{0} & \mathbf{0} & \mathbf{0} & \mathbf{0} & \mathbf{0} \\ C(\boldsymbol{\rho}_t^c) & B(\boldsymbol{\rho}_t^c) & C(\boldsymbol{\rho}_t^c) & \mathbf{0} & \mathbf{0} & \mathbf{0} & \mathbf{0} & \mathbf{0} \\ \mathbf{0} & C(\boldsymbol{\rho}_t^c) & B(\boldsymbol{\rho}_t^c) & C(\boldsymbol{\rho}_t^c) & \mathbf{0} & \mathbf{0} & \mathbf{0} & \mathbf{0} \\ \mathbf{0} & \mathbf{0} & C(\boldsymbol{\rho}_t^c) & B(\boldsymbol{\rho}_t^c) & C(\boldsymbol{\rho}_t^c) & \mathbf{0} & \mathbf{0} & \mathbf{0} \\ \mathbf{0} & \mathbf{0} & \mathbf{0} & C(\boldsymbol{\rho}_t^c) & B(\boldsymbol{\rho}_t^c) & C(\boldsymbol{\rho}_t^c) & \mathbf{0} & \mathbf{0} \\ \mathbf{0} & \mathbf{0} & \mathbf{0} & \mathbf{0} & C(\boldsymbol{\rho}_t^c) & B(\boldsymbol{\rho}_t^c) & C(\boldsymbol{\rho}_t^c) & \mathbf{0} \\ \mathbf{0} & \mathbf{0} & \mathbf{0} & \mathbf{0} & \mathbf{0} & C(\boldsymbol{\rho}_t^c) & B(\boldsymbol{\rho}_t^c) & C(\boldsymbol{\rho}_t^c) \\ \mathbf{0} & \mathbf{0} & \mathbf{0} & \mathbf{0} & \mathbf{0} & \mathbf{0} & C(\boldsymbol{\rho}_t^c) & B(\boldsymbol{\rho}_t^c) \end{bmatrix}, \quad (12)$$

with $B(\boldsymbol{\rho}_t^c)$ and $C(\boldsymbol{\rho}_t^c)$ being block matrices defined as

$$B(\boldsymbol{\rho}_t^c) = \begin{bmatrix} \rho_0^c(t) & \rho_1^c(t) & 0 & 0 \\ \rho_1^c(t) & \rho_0^c(t) & \rho_1^c(t) & 0 \\ 0 & \rho_1^c(t) & \rho_0^c(t) & \rho_1^c(t) \\ 0 & 0 & \rho_1^c(t) & \rho_0^c(t) \end{bmatrix}, \quad (13)$$

$$C(\boldsymbol{\rho}_t^c) = \begin{bmatrix} \rho_1^c(t) & \rho_2^c(t) & 0 & 0 \\ \rho_2^c(t) & \rho_1^c(t) & \rho_2^c(t) & 0 \\ 0 & \rho_2^c(t) & \rho_1^c(t) & \rho_2^c(t) \\ 0 & 0 & \rho_2^c(t) & \rho_1^c(t) \end{bmatrix}. \quad (14)$$

A similar relationship as Eq. (11) holds for the wind velocity amplitude, $\boldsymbol{\alpha}(t)$, and wind velocity angle, $\boldsymbol{\theta}(t)$. Thus, we have

$$\boldsymbol{\alpha}(t) = A^{(\alpha)}(\boldsymbol{\rho}_t^\alpha)\boldsymbol{\alpha}(t - 1) + \mathbf{u}_\alpha(t), \quad (15)$$

$$\boldsymbol{\theta}(t) = A^{(\theta)}(\boldsymbol{\rho}_t^\theta)\boldsymbol{\theta}(t - 1) + \mathbf{u}_\theta(t). \quad (16)$$

Here $\mathbf{u}_\alpha(t)$ and $\mathbf{u}_\theta(t)$ are, respectively the driving processes for amplitude and the angle of wind velocity and matrix $A^{(\alpha)}(\boldsymbol{\rho}_t^\alpha)$ and $A^{(\theta)}(\boldsymbol{\rho}_t^\theta)$ with $\boldsymbol{\rho}_t^\alpha = [\rho_0^\alpha(t), \rho_1^\alpha(t), \rho_2^\alpha(t)]^T$ and $\boldsymbol{\rho}_t^\theta = [\rho_0^\theta(t), \rho_1^\theta(t), \rho_2^\theta(t)]^T$, defined in a similar manner as $A^{(c)}(\boldsymbol{\rho}_t^c)$. The sources which generate these fields are assumed to be independent and therefore these models are decoupled.

Combining these decoupled equations yields the following linear state equation:

$$\mathbf{c}(t) = A^{(c)}(\boldsymbol{\rho}_t^c)\mathbf{c}(t - 1) + \mathbf{u}_c(t), \quad (11)$$

where $\mathbf{u}_c(t) = [u_c([1, 1], t), \dots, u_c([I, J], t)]^T$ is the column vector of the sound speed driving process, and $\boldsymbol{\rho}_t^c = [\rho_0^c(t), \rho_1^c(t), \rho_2^c(t)]^T$ is the associated model parameter vector. Matrix $A^{(c)}(\boldsymbol{\rho}_t^c)$ is a block Toeplitz matrix with Toeplitz blocks, and is defined as the right-stochastic (each row is normalized by the sum of the elements to account for the cells around the boundaries that do not have full support) of the matrix $A^{(c)}(\boldsymbol{\rho}_t^c)$ which for a 4×8 grid is defined as

$$\mathbf{x}_t = A(\boldsymbol{\rho}_t)\mathbf{x}_{t-1} + \mathbf{u}_t, \quad (17)$$

where $\mathbf{u}_t = [\mathbf{u}_c(t)^T, \mathbf{u}_\alpha(t)^T, \mathbf{u}_\theta(t)^T]^T$ is the augmented driving noise vector which is assumed to be Gaussian with zero mean and known covariance matrix, R_u , $\boldsymbol{\rho}_t = [(\boldsymbol{\rho}_t^c)^T, (\boldsymbol{\rho}_t^\alpha)^T, (\boldsymbol{\rho}_t^\theta)^T]^T$ and matrix $A(\boldsymbol{\rho}_t)$ is

$$A(\boldsymbol{\rho}_t) = \begin{bmatrix} A^{(c)}(\boldsymbol{\rho}_t^c) & \mathbf{0}_{IJ \times IJ} & \mathbf{0}_{IJ \times IJ} \\ \mathbf{0}_{IJ \times IJ} & A^{(\alpha)}(\boldsymbol{\rho}_t^\alpha) & \mathbf{0}_{IJ \times IJ} \\ \mathbf{0}_{IJ \times IJ} & \mathbf{0}_{IJ \times IJ} & A^{(\theta)}(\boldsymbol{\rho}_t^\theta) \end{bmatrix}, \quad (18)$$

where $\mathbf{0}_{IJ \times IJ}$ is the zero matrix of size $IJ \times IJ$. Note that the model parameter vector $\boldsymbol{\rho}_t$ is unknown and is to be estimated by the dual UKF algorithm described in the next section.

The relationship between state \mathbf{x}_t and observation vector \mathbf{y}_t at time t is given by Eq. (5) and can be expressed as a nonlinear function of the state variables, i.e.,

$$\mathbf{y}_t = \mathbf{h}(\mathbf{x}_t) + \mathbf{v}_t, \quad (19)$$

where \mathbf{v}_t stands for measurement noise caused by factors such as (i) errors inherent in the gridding process, (ii) error in measuring the travel times, (iii) sensor location error, and (iv) imperfect synchronization across all nodes. This noise is assumed to be a Gaussian random vector with zero mean and known covariance matrix, R_v . The most dominant source for this error is (i). The nonlinear function $\mathbf{h}(\mathbf{x}_t)$ is explicitly defined as

$$\mathbf{h}(\mathbf{x}_t) = \begin{bmatrix} \sum_{i=1}^I \sum_{j=1}^J \frac{d_1(i, j)}{\xi_1([i, j], t) c([i, j], t) + \mathbf{s}_1([i, j], t) \cdot \mathbf{v}([i, j], t)} \\ \vdots \\ \sum_{i=1}^I \sum_{j=1}^J \frac{d_N(i, j)}{\xi_N([i, j], t) c([i, j], t) + \mathbf{s}_N([i, j], t) \cdot \mathbf{v}([i, j], t)} \end{bmatrix}. \quad (20)$$

III. DUAL STATE-PARAMETER ESTIMATION USING UNSCENTED KALMAN FILTER

In a state-space problem, if the state and the model parameters are both unknown, then the problem of estimating state and model parameters from the observation is known as a dual estimation problem. There are in general two different approaches toward solving a nonlinear dual state-parameter estimation problem using UKF, namely, joint UKF (Refs. 21 and 22) and dual UKF.^{15,16,21} A comparative study of the joint and dual UKFs can be found in Refs. 21 and 22 in which it is

shown that these filters perform very closely in reconstruction accuracy. In this paper the dual UKF is chosen over the joint UKF due to its perspicuous formulation.

In the dual UKF,¹⁶ two decoupled UKFs run simultaneously, one for state estimation and the other for the parameter estimation. At every time snapshot, the current estimate of the model parameter vector is used in the state estimation whereas the current estimate of the state vector is used in the parameter estimation. Therefore, the acoustic tomography of the atmosphere using dual UKF can be formulated as follows:

$$\text{dual UKF : } \begin{cases} \text{state UKF : } & \begin{cases} \mathbf{x}_t = \mathbf{A}(\hat{\boldsymbol{\rho}}_{t-1|t-1})\mathbf{x}_{t-1} + \mathbf{u}_t, \\ \mathbf{y}_t = \mathbf{h}(\mathbf{x}_t) + \mathbf{v}_t, \end{cases} \\ \text{parameter UKF : } & \begin{cases} \boldsymbol{\rho}_t = \boldsymbol{\rho}_{t-1} + \mathbf{n}_t, \\ \mathbf{y}_t = \mathbf{h}(\mathbf{A}(\boldsymbol{\rho}_t)\hat{\mathbf{x}}_{t-1|t-1}) + \mathbf{v}_t, \end{cases} \end{cases} \quad (21)$$

where $\hat{\boldsymbol{\rho}}_{t-1|t-1}$ and $\hat{\mathbf{x}}_{t-1|t-1}$ are the model parameter vector and the state vector estimates at time $t-1$, respectively, and \mathbf{n}_t is the model parameter driving noise process which is assumed to be Gaussian and independent of both \mathbf{v}_t and \mathbf{u}_t . Note that we start from the straight ray model and update $\xi_n([\cdot, \cdot], t+1)$ for all n based on the reconstructed temperature and wind velocity at time t . The schematic diagram of the dual UKF is illustrated in Fig. 3.

Assuming that the covariance matrices of the state evolution driving noise, \mathbf{R}_u , model parameter driving noise, \mathbf{R}_n , and the observation noise \mathbf{R}_v are known (or can be estimated), the dual UKF steps to estimate the state and model parameters are as follows.

(1) Initialization: The dual UKF starts by initializing the state and model parameter vectors estimates $\hat{\mathbf{x}}_{0|0}$ and $\hat{\boldsymbol{\rho}}_{0|0}$, respectively. Here, $\hat{\mathbf{x}}_{0|0}$ is initialized to the mean fields estimated from travel times using the method explained in Ref. 8 and the model parameter vector is initialized to $\hat{\boldsymbol{\rho}}_{0|0} = [1, 0, 0, 1, 0, 0, 1, 0, 0]^T$ which corresponds to a random walk model. In addition, the corresponding state error covariance matrices $\mathbf{P}_{0|0}^x$ and $\mathbf{P}_{0|0}^\rho$ are initialized with identity matrices.

(2) *A priori* state and parameter estimation: Since the state and model parameter evolution models are linear, the *a priori* state, $\hat{\mathbf{x}}_{t|t-1}$, model parameter, $\hat{\boldsymbol{\rho}}_{t|t-1}$, and the corresponding *a priori* error covariance matrices $\mathbf{P}_{t|t-1}^x$ and $\mathbf{P}_{t|t-1}^\rho$ are calculated as

$$a \text{ priori state estimation : } \begin{cases} \hat{\mathbf{x}}_{t|t-1} = \mathbf{A}(\hat{\boldsymbol{\rho}}_{t-1|t-1})\hat{\mathbf{x}}_{t-1|t-1}, \\ \mathbf{P}_{t|t-1}^x = \mathbf{A}(\hat{\boldsymbol{\rho}}_{t-1|t-1})\mathbf{P}_{t-1|t-1}^x \mathbf{A}^T(\hat{\boldsymbol{\rho}}_{t-1|t-1}) + \mathbf{R}_u, \end{cases} \quad (22)$$

$$a \text{ priori parameter estimation : } \begin{cases} \hat{\boldsymbol{\rho}}_{t|t-1} = \hat{\boldsymbol{\rho}}_{t-1|t-1}, \\ \mathbf{P}_{t|t-1}^\rho = \mathbf{P}_{t-1|t-1}^\rho + \mathbf{R}_n. \end{cases} \quad (23)$$

(3) Sigma point generation: Due to the nonlinearity of the observation process, unscented transform is used to estimate the distribution of the observation vector. State and model parameter sigma points are calculated based on $\hat{\mathbf{x}}_{t|t-1}$, $\hat{\boldsymbol{\rho}}_{t|t-1}$, $\mathbf{P}_{t|t-1}^x$, and $\mathbf{P}_{t|t-1}^\rho$ and subsequently fed into the nonlinear function $\mathbf{h}(\cdot)$ in order to derive the estimate of the measurement vector, $\hat{\mathbf{y}}_{k|k-1}(t)$,

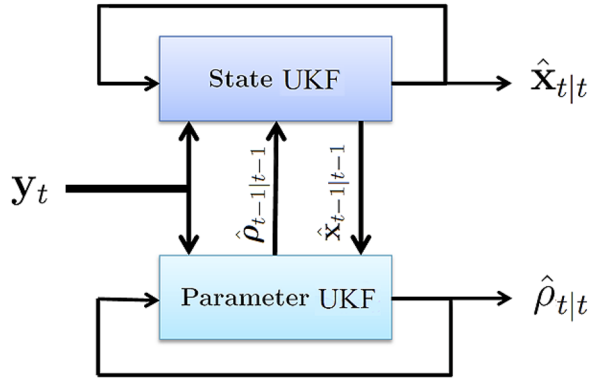


FIG. 3. (Color online) Schematic diagram of the dual UKF method used for simultaneous state and parameter estimation to account for time-varying nature of the model.

$$\text{state sigma points : } \begin{cases} \chi_0^x(t) = \hat{\mathbf{x}}_{t|t-1}, \\ \chi_i^x(t) = \hat{\mathbf{x}}_{t|t-1} + \gamma \sqrt{\mathbf{P}_{t|t-1}^x}_{[i]}, \\ \chi_{L+i}^x(t) = \hat{\mathbf{x}}_{t|t-1} - \gamma \sqrt{\mathbf{P}_{t|t-1}^x}_{[i]}, \end{cases} \quad (24)$$

$$\text{parameter sigma points : } \begin{cases} \chi_0^\rho(t) = \hat{\rho}_{t|t-1}, \\ \chi_i^\rho(t) = \hat{\rho}_{t|t-1} + \gamma \sqrt{\mathbf{P}_{t|t-1}^\rho}_{[i]}, \\ \chi_{L+i}^\rho(t) = \hat{\rho}_{t|t-1} - \gamma \sqrt{\mathbf{P}_{t|t-1}^\rho}_{[i]} \end{cases} \quad (25)$$

for $i = 1, \dots, L$, where $\gamma \approx \varrho\sqrt{L}$ is a scaling parameter and ϱ determines the spread of sigma points, and $\sqrt{\mathbf{P}_{t|t-1}^x}_{[i]}$ and $\sqrt{\mathbf{P}_{t|t-1}^\rho}_{[i]}$ are the i th columns of the Cholesky factors of covariance matrices $\mathbf{P}_{t|t-1}^x$ and $\mathbf{P}_{t|t-1}^\rho$, respectively.

The new sigma points are transformed through the non-linear observation process Eq. (19), to yield

$$\mathbf{Y}_i^x(t) = \mathbf{h}(\chi_i^x(t)), \quad i = 0, \dots, 2L, \quad (26)$$

$$\mathbf{Y}_i^\rho(t) = \mathbf{h}(\mathbf{A}(\chi_i^\rho(t)) \hat{\mathbf{x}}_{t-1|t-1}), \quad i = 0, \dots, 2L. \quad (27)$$

- (4) Covariance matrices computation: The transformed sigma points $\mathbf{Y}_i^x(t)$ and $\mathbf{Y}_i^\rho(t)$ are then used to find observation vector estimates for state and parameter filters $\hat{\mathbf{y}}_{t|t-1}^x$ and $\hat{\mathbf{y}}_{t|t-1}^\rho$ and the corresponding covariance and cross-covariance matrices $\mathbf{P}_{yy}^x(t)$, $\mathbf{P}_{xy}^x(t)$, $\mathbf{P}_{yy}^\rho(t)$, and $\mathbf{P}_{xy}^\rho(t)$ using

$$\text{for state filter: } \begin{cases} \hat{\mathbf{y}}_{t|t-1}^x = \sum_{i=0}^{2L} W_i^{(m)} \mathbf{Y}_i^x(t), \\ \mathbf{P}_{yy}^x(t) = \sum_{i=0}^{2L} W_i^{(c)} [\mathbf{Y}_i^x(t) - \hat{\mathbf{y}}_{t|t-1}^x] [\mathbf{Y}_i^x(t) - \hat{\mathbf{y}}_{t|t-1}^x]^T + R_v, \\ \mathbf{P}_{xy}^x(t) = \sum_{i=0}^{2L} W_i^{(c)} [\chi_i^x(t) - \hat{\mathbf{x}}_{t|t-1}] [\mathbf{Y}_i^x(t) - \hat{\mathbf{y}}_{t|t-1}^x]^T, \end{cases} \quad (28)$$

$$\text{for parameter filter: } \begin{cases} \hat{\mathbf{y}}_{t|t-1}^\rho = \sum_{i=0}^{2L} W_i^{(m)} \mathbf{Y}_i^\rho(t), \\ \mathbf{P}_{yy}^\rho(t) = \sum_{i=0}^{2L} W_i^{(c)} [\mathbf{Y}_i^\rho(t) - \hat{\mathbf{y}}_{t|t-1}^\rho] [\mathbf{Y}_i^\rho(t) - \hat{\mathbf{y}}_{t|t-1}^\rho]^T + R_v, \\ \mathbf{P}_{\rho y}^\rho(t) = \sum_{i=0}^{2L} W_i^{(c)} [\chi_i^\rho(t) - \hat{\rho}_{t|t-1}] [\mathbf{Y}_i^\rho(t) - \hat{\mathbf{y}}_{t|t-1}^\rho]^T, \end{cases} \quad (29)$$

where the weights $W_i^{(m)}$ s and $W_i^{(c)}$ s are²³ $W_0^{(m)} = \lambda/(\lambda + L)$, $W_0^{(c)} = \lambda/(\lambda + L) + (1 - \varrho^2 + \beta)$, and $W_i^{(m)} = W_i^{(c)} = 1/2(K + \lambda)$ for $i = 1, \dots, 2L$ with β being a constant used to incorporate prior knowledge of the distribution of the state vector and is set to $\beta = 2$ for Gaussian distributions, and $\lambda = L(\varrho^2 - 1)$ is a scaling parameter.

- (5) *A posteriori* state/parameter estimation: These are used to generate the Kalman gain matrices for the state and parameter filters, \mathbf{K}_t^x and \mathbf{K}_t^ρ , the *a posteriori* state and parameter vectors, $\hat{\mathbf{x}}_{t|t}$ and $\hat{\rho}_{t|t}$, and the *a posteriori* error covariance matrices, $\mathbf{P}_{t|t}^x$ and $\mathbf{P}_{t|t}^\rho$, using

$$\text{a posteriori state estimation: } \begin{cases} \mathbf{K}_t^x = \mathbf{P}_{xy}^x(t) (\mathbf{P}_{yy}^x(t))^{-1}, \\ \hat{\mathbf{x}}_{t|t} = \hat{\mathbf{x}}_{t|t-1} + \mathbf{K}_t^x [\mathbf{y}_t - \hat{\mathbf{y}}_{t|t-1}^x], \\ \mathbf{P}_{t|t}^x = \mathbf{P}_{t|t-1}^x - \mathbf{K}_t^x \mathbf{P}_{yy}^x(t) \mathbf{K}_t^{xT}, \end{cases} \quad (30)$$

$$a \text{ posteriori parameter estimation : } \begin{cases} \mathbf{K}_t^\rho = \mathbf{P}_{\rho y}(t)(\mathbf{P}_{yy}^\rho(t))^{-1}, \\ \hat{\boldsymbol{\rho}}_{t|t} = \hat{\boldsymbol{\rho}}_{t|t-1} + \mathbf{K}_t^\rho [\mathbf{y}_t - \hat{\mathbf{y}}_{t|t-1}^\rho], \\ \mathbf{P}_{t|t}^\rho = \mathbf{P}_{t|t-1}^\rho - \mathbf{K}_t^\rho \mathbf{P}_{yy}^\rho(t) \mathbf{K}_t^{\rho T}. \end{cases} \quad (31)$$

Note that $\hat{\mathbf{x}}_{t|t}$, $\hat{\boldsymbol{\rho}}_{t|t}$, $\mathbf{P}_{t|t}^x$, and $\mathbf{P}_{t|t}^\rho$ are used as the prior estimates at time $t + 1$. Finally, assuming $\mathbf{n}_n([i, j], t)$ can be measured, the path of the acoustic wave is updated as follows:

$$s_n([i, j], t + 1) = \frac{\mathbf{n}_n([i, j], t) \hat{c}([i, j], t|t) + \hat{\mathbf{v}}([i, j], t|t)}{\|\mathbf{n}_n([i, j], t) \hat{c}([i, j], t|t) + \hat{\mathbf{v}}([i, j], t|t)\|}. \quad (32)$$

IV. EXPERIMENTAL RESULTS

In order to test our proposed UKF-based dual state-parameter estimation algorithm a data set was acquired from the University of Leipzig. This data set was collected at the Meteorological Observatory, Lindenberg, Germany, as part of the STINHO project.¹⁸ The experiment was part of a larger meteorological experiment to study turbulence, turbulent fluxes, and other meteorological parameters. In this experiment, the investigation area was of the size $300 \text{ m} \times 440 \text{ m}$ and the tomography array consisted of eight acoustic transmitters, $S1, \dots, S8$, and twelve receivers, $R1, \dots, R12$. Most of the ground within the tomography array was covered with grass except for a spot of plowed land which was in the lower left corner of the field and of size $90 \text{ m} \times 300 \text{ m}$. Figure 4 shows the investigation field, the grass covered and plowed land areas, and the locations of the transmitters and receivers.

In this experiment the underlying topography of the field was not homogenous, i.e., there were relatively large fluctuations in the elevations ($0 \leq h \leq 6.6 \text{ m}$). Therefore, the sensors

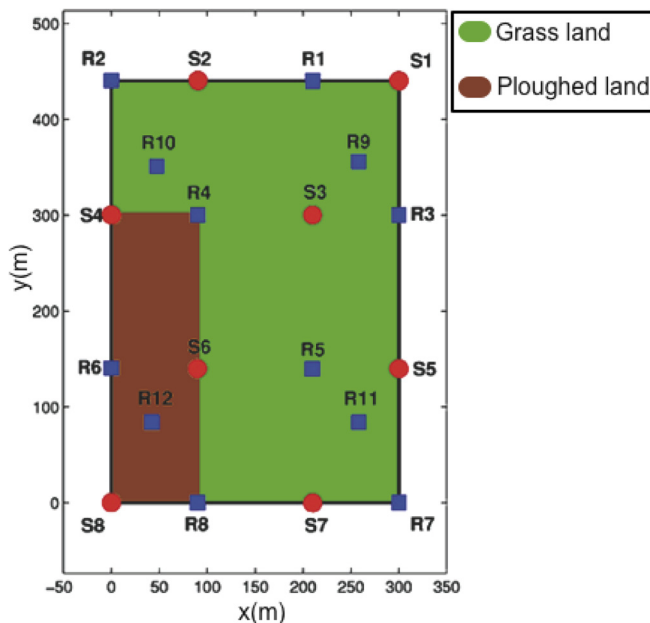


FIG. 4. (Color online) STINHO experimental setup shows the size of the field, grass and plowed land areas, and the distribution pattern of the acoustic sensor nodes (transmitters and receivers).

had to be elevated at different heights in order to assure that they are approximately on the same horizontal plane about 2 m above the ground. The acoustic travel times for all paths were then measured on July 6th, 2002 for 1038 snapshots at one minute intervals on 000-1717 UTC. The data set has considerable missing/bad measurements. The travel time measurements for 17 out of 96 transmitter-receiver paths were excluded at all snapshots. These corresponded to long paths that violated straight-ray assumption. Additionally, at certain snapshots the sensors exhibit missing data intermittently, which could be due to equipment malfunction, missed detections, or very low signal-to-noise ratio (SNR). Figure 5 illustrates the matrix of travel time measurements over all snapshots as a binary matrix in which “1” represents missing data (white) while “0” denotes no missing data (black). A more detailed explanation of this experiment can be found in Ref. 18.

The intermittent missing data imply that the dimension of the observation vector in Eq. (9) changes at different times. In order to deal with such inconsistency in the number of measurements, the observation function in Eq. (19) and the measurement noise \mathbf{v}_t are adjusted at every snapshot to fit the measured data. This is accomplished by labeling the missing path at each snapshot and removing them from Eq. (20), as well as changing the size of the measurement noise to the number of observed data, N_m .

The first 300 snapshots (5 h) of the data are missing relatively lesser number of measurements. Thus, this portion of the data was used to evaluate the performance of the proposed method. A 4×8 grid is overlaid on the investigation area to partition the field into 32 grids of dimensions $75 \text{ m} \times 55 \text{ m}$ each. There were two *in situ* measurements for temperature and one for wind velocity using a sonic anemometer^{18,24} located at 2 m height on a 10 m mast. The locations of the two temperature sensors correspond to grids $[i = 1, j = 4]$, $[i = 3, j = 5]$ while the anemometer is located

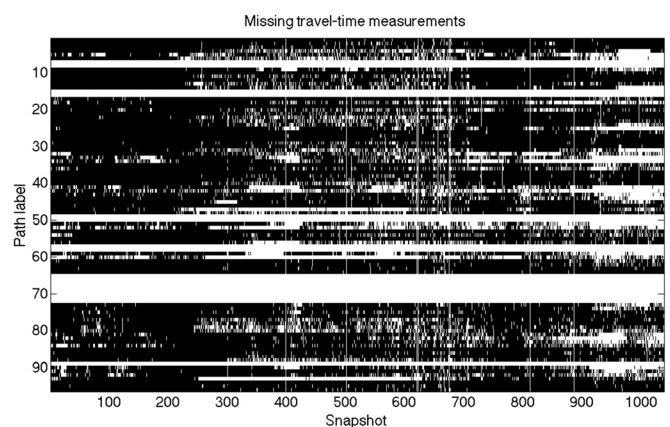


FIG. 5. Missing travel time measurements (indicated in white) in STINHO data for each path as a function of time (snapshot).

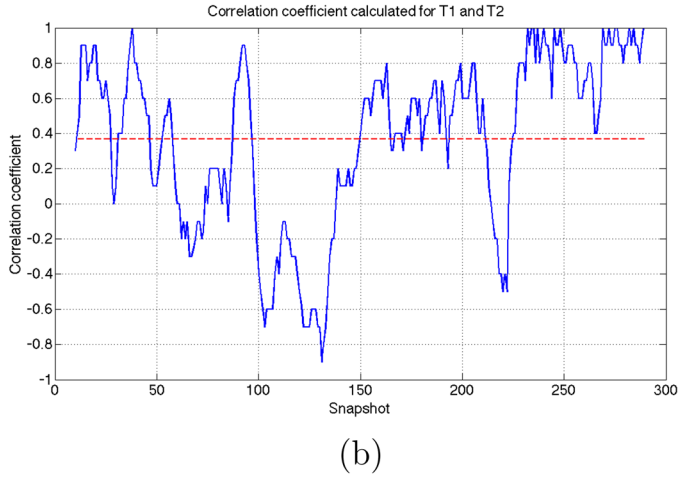
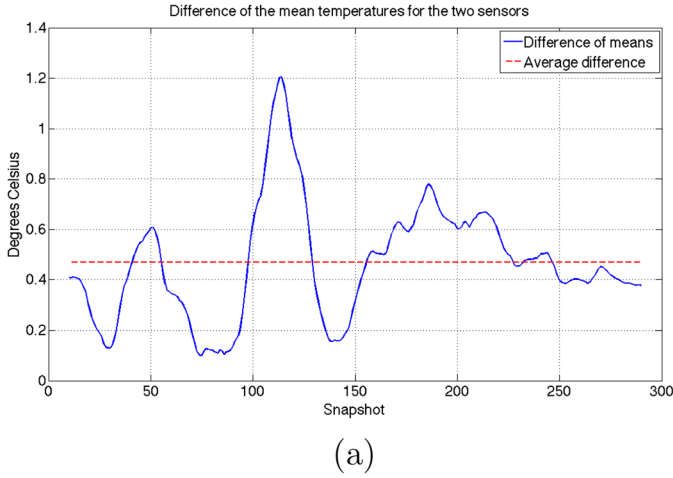


FIG. 6. (Color online) (a) The difference of mean temperature values at the two *in situ* sensors and (b) correlation coefficient of the two *in situ* measurements. The dotted lines show the averaged values over all snapshots.

at grid $[i=2, j=8]$. The mean of the measured temperature values as well as the correlation coefficient between the two measured temperature values at grids $[i=1, j=4]$, $[i=3, j=5]$ are calculated over moving windows of size 20. Figures 6(a) and 6(b) show the difference between the calculated mean temperature values and the correlation coefficient, respectively. The correlation coefficient plot indicates the fact that for the choice of spatial grid resolution, the sensors are not highly correlated temporally and hence, the size of the grid is indeed not coarse.

For the first snapshot mean temperature and wind velocity fields are calculated from the measured travel times using the method explained in Ref. 8. As mentioned before, owing to low wind conditions during the data collection process it is assumed that $\mathbf{s} \cdot \mathbf{n} = 1$. The estimated mean fields are used as initial state vector, $\hat{\mathbf{x}}_{0|0}$. The initial model parameter vector is set to $\hat{\rho}_{0|0} = [1, 0, 0, 1, 0, 0, 1, 0, 0]^T$, which corresponds to starting from a random walk model for all fields. Furthermore, the state and parameter error covariance matrices are taken to be $\mathbf{P}_{0|0}^x = \mathbf{I}_{96 \times 96}$ and $\mathbf{P}_{0|0}^\rho = \mathbf{I}_{9 \times 9}$, respectively. It is assumed that \mathbf{v}_r , \mathbf{u}_r , and \mathbf{n}_r are mutually uncorrelated, zero mean Gaussian processes with covariance matrices $\mathbf{R}_v = \sigma_v^2 \mathbf{I}$, \mathbf{R}_u , and \mathbf{R}_n , respectively, where $\sigma_v^2 = 0.01$ is chosen based upon the uncertainty measurement reported in Ref. 18 which is 0.3 ms for each measurement. Covariance matrix \mathbf{R}_n is assumed to be diagonal of the form $\mathbf{R}_n = \text{diag}[\sigma_0^2, \sigma_1^2, \sigma_2^2, \sigma_0^2, \sigma_1^2, \sigma_2^2, \sigma_0^2, \sigma_1^2, \sigma_2^2]$, where based on our experiments with the synthetic data set generated in Ref. 8, the diagonal values are chosen to be $\sigma_0^2 = 0.0025$, $\sigma_1^2 = 0.0005$, and $\sigma_2^2 = 0.0001$. The driving noise is assumed to be a zero mean white Gaussian process with covariance matrix, $\mathbf{R}_u = \sigma_u^2 \mathbf{I}$ where $\sigma_u^2 = 0.0025$ is also chosen based on the experiment on the synthetic data.

Having the covariance matrices \mathbf{R}_v , \mathbf{R}_u , and \mathbf{R}_n , and the initial values $\hat{\mathbf{x}}_{0|0}$, $\hat{\rho}_{0|0}$, $\mathbf{P}_{0|0}^x$, and $\mathbf{P}_{0|0}^\rho$ the states (fields) and model parameters are simultaneously estimated at every snapshot, t , using the dual UKF method in the previous section. Figures 7(a)–7(c) show the estimated model parameters $\hat{\rho}_{t|t} = [\hat{\rho}_0^c(t), \hat{\rho}_1^c(t), \hat{\rho}_2^c(t), \hat{\rho}_0^z(t), \hat{\rho}_1^z(t), \hat{\rho}_2^z(t), \hat{\rho}_0^\theta(t), \hat{\rho}_1^\theta(t), \hat{\rho}_2^\theta(t)]$ calculated using Eq. (31) for temperature, wind

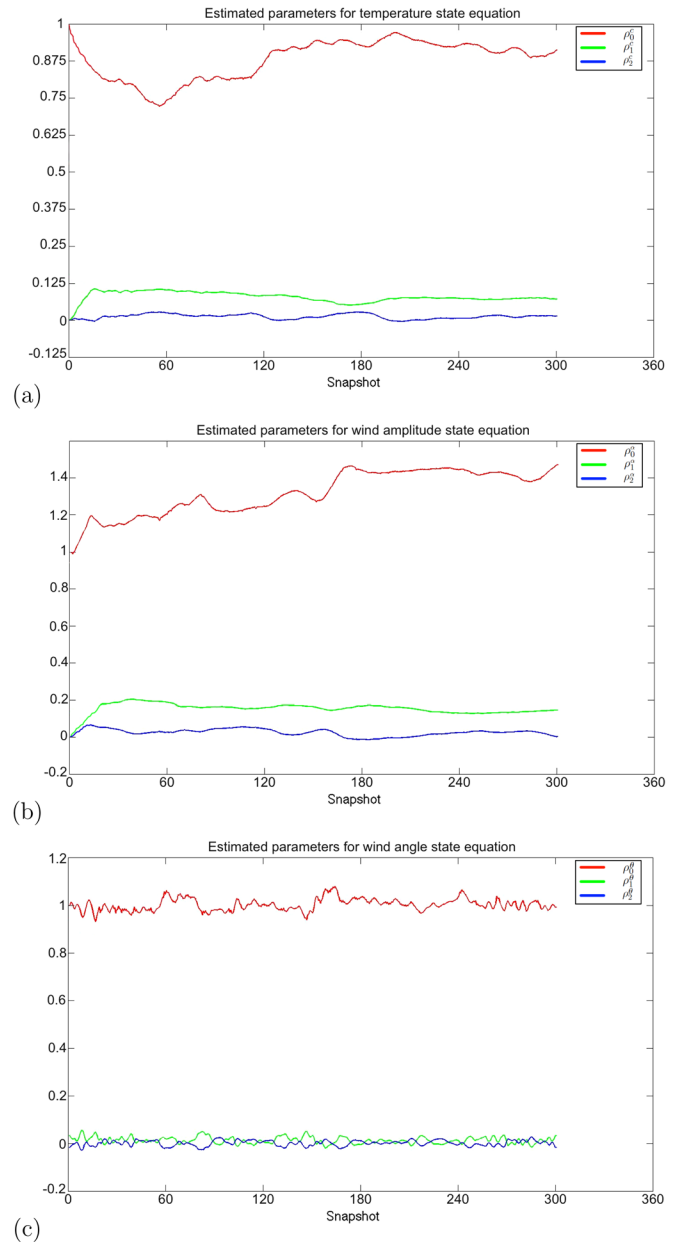


FIG. 7. (Color online) The estimated parameters for (a) temperature, (b) wind velocity, and (c) wind angle.

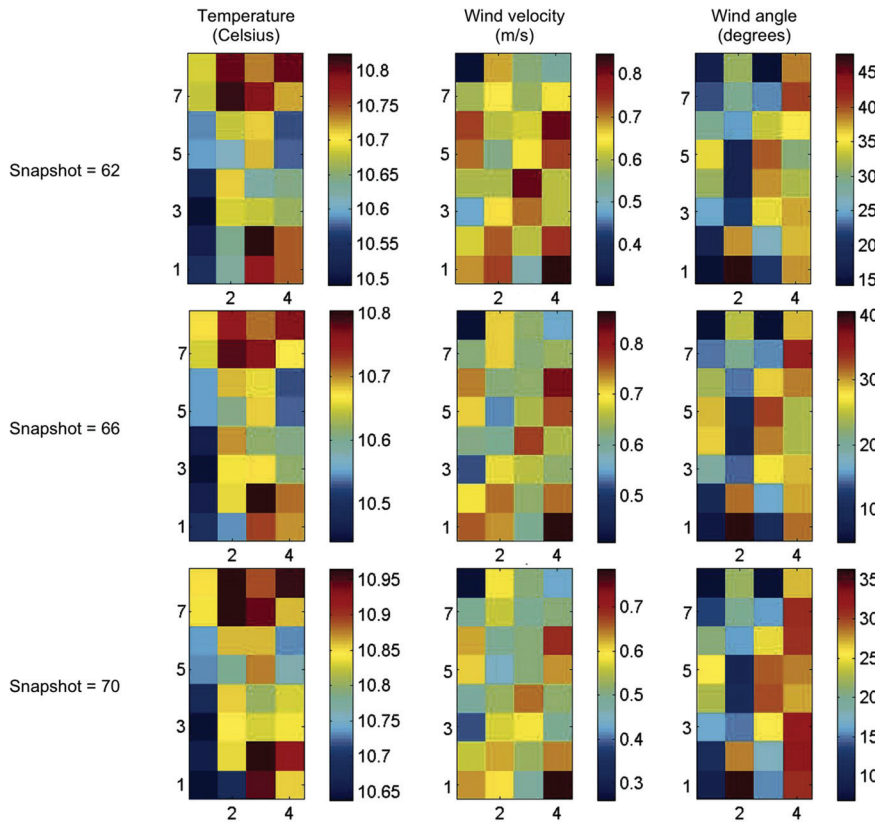


FIG. 8. Reconstructed temperature and wind velocity fields using the proposed dual UKF method at each grid for snapshots $t = \{62, 66, 70\}$.

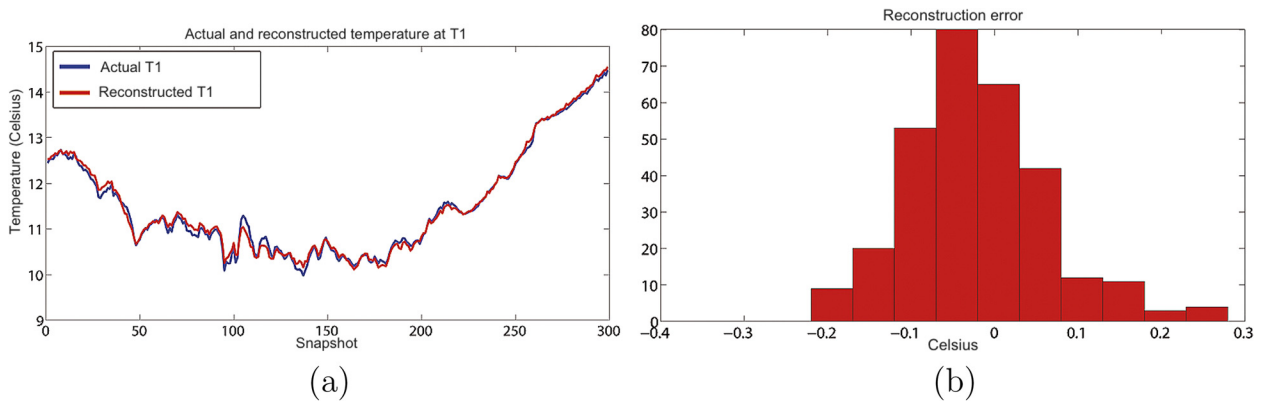


FIG. 9. (Color online) (a) Actual measured and reconstructed temperature at the grid $[i = 1, j = 4]$ (b) Reconstruction error histogram shows mean error of approximately -0.02 and standard deviation of 0.09 °C.

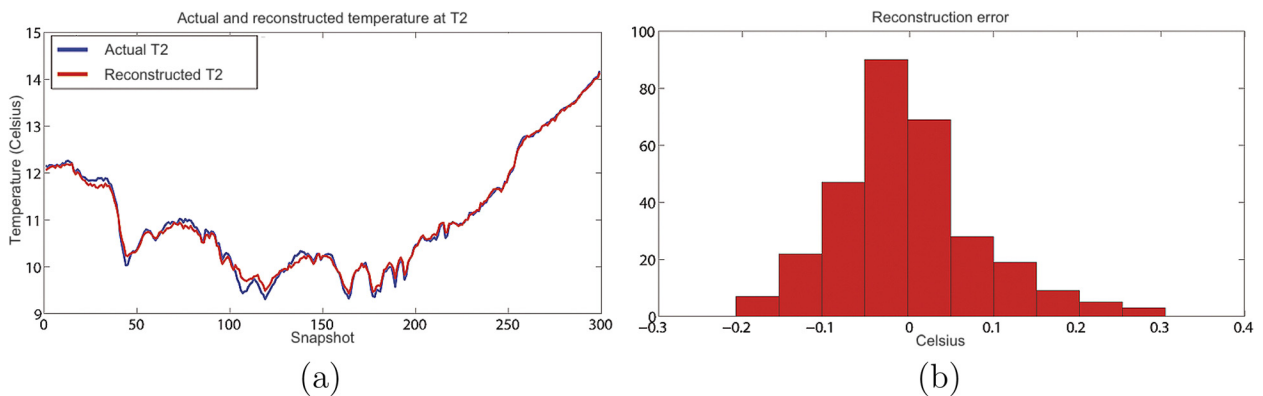


FIG. 10. (Color online) (a) Actual measured and reconstructed temperature at the grid $[i = 3, j = 5]$ (b) Reconstruction error histogram shows mean error of approximately -0.02 and standard deviation of 0.09 °C.

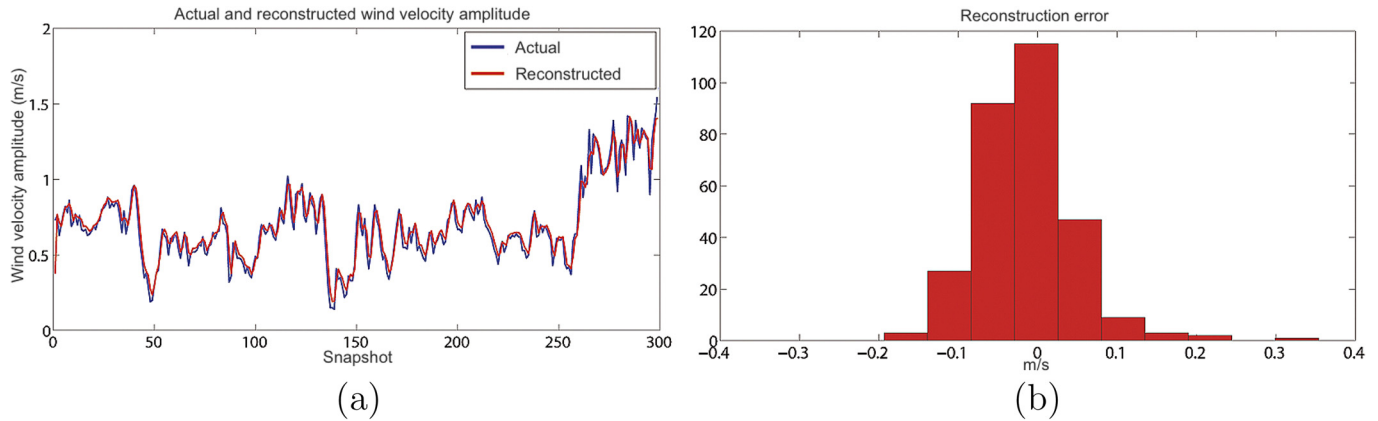


FIG. 11. (Color online) Actual measured and reconstructed wind velocity amplitude at the grid $[i = 2, j = 8]$ (b) Reconstruction error histogram shows mean error of approximately -0.01 and standard deviation of 0.06 m/s.

velocity amplitude, and wind velocity angle, respectively. As can be seen that these parameters initially start from random walk and are continuously tracked in time for the first 300 snapshots of the data. Moreover, our observations from Fig. 7(c) suggest that the wind velocity angle parameters, in this experiment, follow closely a random walk behavior. We believe this phenomenon is due to the fact that the temporal snapshots are coarse in time.

Figure 8 shows the reconstructed temperature and wind velocity fields at snapshots 62, 66, and 70, respectively. As can be seen from these results, the reconstructed fields over this time period are consistent and changing gradually, as expected. In addition, it can be seen that the proposed method has captured the temperature difference between the grassland and plowed land portions. Note that the reconstructed temperature fields at the snapshots in Fig. 8 indicate variation of about 0.4°C , which is in agreement with the results provided in Fig. 6.

In order to evaluate the reconstruction accuracy of the proposed method, the reconstructed temperature at grids $[i = 1, j = 4]$ and $[i = 3, j = 5]$, and the reconstructed wind velocity amplitude and angle at grid $[i = 2, j = 8]$ are compared to those reported from *in situ* measurements. Figures 9 and 10 show the reported and reconstructed temperature

based on temperature *in situ* measurements, and Figs. 11 and 12 show the reported and reconstructed wind velocity amplitude and angle for the first 300 snapshots together with the histogram of the reconstruction errors for these snapshots. As can be seen from these figures, the reconstructed fields generated using the UKF-based dual state-parameter estimation approach are in good agreements with the *in situ* measurements. Note that in Fig. 12, the jump at snapshot 81 is due to the fact that the angle becomes negative and is folded over by $360 + \theta$. The average temperature reconstruction errors at grids $[i = 3, j = 5]$ and $[i = 1, j = 4]$ using our proposed method are calculated to be around $\mu = -0.02^\circ\text{C}$ with the standard deviation of $\sigma = 0.09^\circ\text{C}$ and $\mu = -0.01^\circ\text{C}$ with the standard deviation of $\sigma = 0.08^\circ\text{C}$, respectively. Moreover, the average wind velocity amplitude and angle reconstruction errors (at grid $[i = 2, j = 8]$) are calculated to be $\mu = -0.01$ m/s with standard deviation of $\sigma = 0.06$ m/s and $\mu = 0.38^\circ$ with standard deviation of $\sigma = 2.6^\circ$, respectively.

Comparing the reconstructed fields with the *in situ* measurements, it can readily be seen that the proposed dual state-parameter estimation method provides accurate temperature and wind velocity reconstructions. The computationally efficiency of the UKF-based method,⁸ its adaptive nature, and

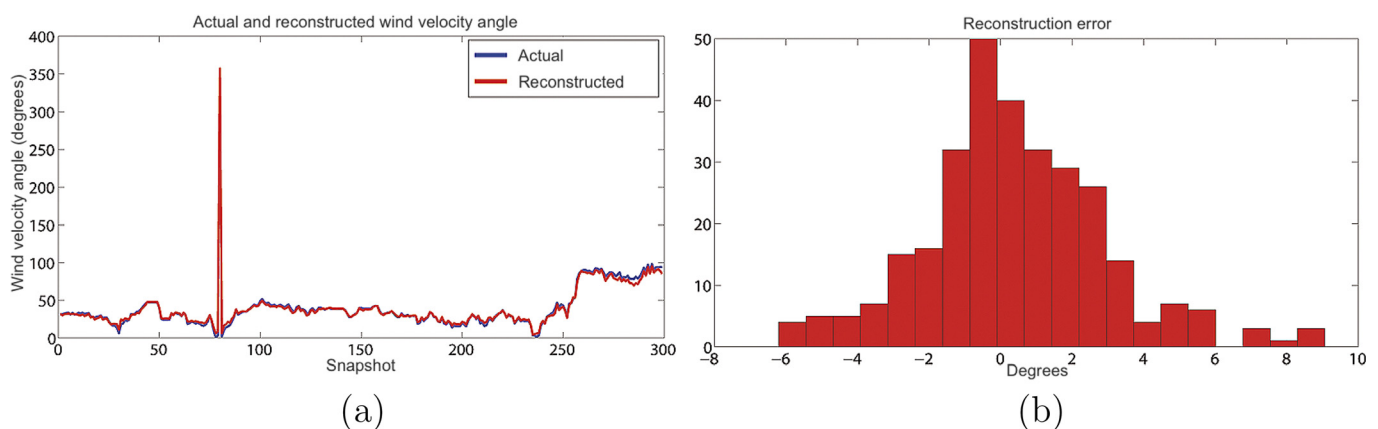


FIG. 12. (Color online) Actual measured and reconstructed wind velocity angle at the grid $[i = 2, j = 8]$. (b) Reconstruction error histogram shows mean error of approximately 0.4° and standard deviation of approximately 2.6° .

its reconstruction accuracy make this method a very good candidate for solving acoustic tomography problems.

V. CONCLUSION

In this paper a new statistical-based approach for acoustic tomography of the atmosphere was proposed in which the problem was formulated as a dual state-parameter estimation. In this approach, the state vectors were formed from the temperature and wind velocity fields in all grids. The parameters of spatial-temporal 3-D AR models used to capture the state evolutions were also assumed to be unknown and time-varying. An iterative ray-tracing algorithm was given to handle situations when the straight-ray assumption can no longer hold. A dual UKF-based method was then employed for this nonlinear state-parameter estimation problem.

The proposed method was applied to the data set collected in the STINHO experiment¹⁸ in order to reconstruct the temperature and wind velocity fields. Owing to low wind conditions in this data set and lack of angle of arrival measurements straight-ray model was assumed hence leading to a linearized observation model with negligible approximation errors. Nevertheless, the proposed dual UKF was employed in order to illustrate how the general problem (bent-ray model) can be solved when the observation equation is nonlinear.

The reconstructed fields were computed and compared with the *in situ* temperature and wind velocity measurements reported in the data set. It was shown that the proposed method is capable of reconstructing the temperature and wind velocity fields with high accuracy and speed. Moreover, due to adaptive nature of this method it can capture the non-stationarity behavior of the temperature and wind velocity fields. More research will be needed to verify the real applicability of the proposed methods in presence of large temperature or wind velocity gradients.

ACKNOWLEDGMENTS

This research was supported by the DoD Center for Geosciences/Atmospheric Research at Colorado State University under Cooperative Agreement No. W911NF-06-2-0015 with the Army Research Laboratory. The acoustic and meteorological measurements were collected as part of the VERTICO (vertical transports of energy and trace gases at anchor stations under complex natural conditions) project funded by the German Federal Ministry of Education and Research (BMBF) under the AFO-2000 research program (Grant No. 07ATF37). We would also like to thank the colleagues in the VERTICO network for their support of the STINHO (structure of turbulent transport under inhomogeneous conditions)-2 experiment, in particular Armin Raabe and Klaus Arnold at the Leipzig Institute for Meteorology, University of Leipzig, for acoustic measurements as well as Thomas Foken and his colleagues at the Department of Micrometeorology, University of Bayreuth, for providing the wind measurements.

¹D. K. Wilson and D. W. Thomson, "Acoustic tomographic monitoring of the atmospheric surface layer," *J. Atmos. Ocean. Technol.* **11**, 751–769 (1994).

- ²D. K. Wilson, A. Ziemann, V. E. Ostashev, and A. G. Voronovich, "An overview of acoustic travel-time tomography in the atmosphere and its potential applications," *Acustica* **87**, 721–730 (2001).
- ³A. Ziemann, K. Arnold, and A. Raabe, "Acoustic travel time tomography—A method for remote sensing of the atmospheric surface layer," *Meteorol. Atmos. Phys.* **71**, 43–51 (1999).
- ⁴K. Arnold, A. Ziemann, A. Raabe, and G. Spindler, "Acoustic tomography and conventional meteorological measurements over heterogeneous surfaces," *Meteorol. Atmos. Phys.* **85**, 175–186 (2004).
- ⁵S. N. Vecherin, V. E. Ostashev, G. H. Goedecke, D. K. Wilson, and A. G. Voronovich, "Time-dependent stochastic inversion in acoustic travel-time tomography of the atmosphere," *J. Acoust. Soc. Am.* **119**, 2579–2588 (2006).
- ⁶S. N. Vecherin, V. E. Ostashev, A. Ziemann, D. K. Wilson, K. Arnold, and M. Barth, "Tomographic reconstruction of atmospheric turbulence with the use of time-dependent stochastic inversion," *J. Acoust. Soc. Am.* **122**, 1416–1425 (2007).
- ⁷V. E. Ostashev, S. N. Vecherin, D. K. Wilson, A. Ziemann, and G. H. Goedecke, "Recent progress in acoustic travel-time tomography of the atmospheric surface layer," *Meteorol. Z.* **18**, 125–133 (2009).
- ⁸S. Kolouri and M. R. Azimi-Sadjadi, "Acoustic tomography of the atmosphere using unscented Kalman filter," in *Signal Processing Conference (EUSIPCO), 2012 Proceedings of the 20th European (IEEE, Bucharest, Romania, 2012)*, pp. 2531–2535.
- ⁹K. Arnold, A. Ziemann, and A. Raabe, "Tomographic monitoring of wind and temperature at different heights above the ground," *Acustica* **87**, 703–708 (2001).
- ¹⁰I. Jovanovic, A. Hormati, L. Sbaiz, and M. Vetterli, "Efficient and stable acoustic tomography using sparse reconstruction methods," in *19th International Congress on Acoustics (2007)*, pp. 1–6.
- ¹¹A. H. Andersen and A. C. Kak, "Simultaneous algebraic reconstruction technique (SART): A superior implementation of the art algorithm," *Ultrasonic Imaging* **6**, 81–94 (1984).
- ¹²L. Scharf, "Statistical signal processing: Detection, estimation, and time series analysis," in *Addison-Wesley Series in Electrical Engineering* (Addison-Wesley, New York, 1991).
- ¹³M. Barth and A. Raabe, "Acoustic tomographic imaging of temperature and flow fields in air," *Meas. Sci. Technol.* **22**, 035102 (2011).
- ¹⁴S. Kodali, K. Deb, P. Munshi, and N. Kishore, "Comparing GA with MART to tomographic reconstruction of ultrasound images with and without noisy input data," in *IEEE Congress on Evolutionary Computation, CEC'09 (2009)*, pp. 2963–2970.
- ¹⁵E. A. Wan, R. Van Der Merwe, and A. T. Nelson, "Dual estimation and the unscented transformation," *Adv. Neural Inf. Process. Syst.* **12**, 666–773 (2000).
- ¹⁶M. C. Vandyke, J. L. Schwartz, and C. D. Hall, "Unscented Kalman filtering for spacecraft attitude state and parameter estimation," in *The AAS/AIAA Space Flight Mechanics Conference, AAS 04-115, Maui, Hawaii (2004)*, pp. 217–228.
- ¹⁷J. H. Gove and D. Y. Hollinger, "Application of a dual unscented Kalman filter for simultaneous state and parameter estimation in problems of surface-atmosphere exchange," *J. Geophys. Res.* **111**, 1–21 (2006).
- ¹⁸A. Raabe, K. Arnold, A. Ziemann, M. Schroeter, S. Raasch, J. Bange, P. Zittel, T. Spiess, T. Foken, M. Goeckede, F. Beyrich, and J. P. Leps, "STINHO, structure of turbulent transport under inhomogeneous surface conditions," *Meteorol. Z.* **14**, 315–327 (2005).
- ¹⁹I. Jovanovic, "Acoustic tomography for scalar and vector fields: Theory and application to temperature and wind estimation," *J. Atmos. Oceanic Technol.* **26**, 1475–1492 (2009).
- ²⁰V. Ostashev, *Acoustics in Moving Inhomogeneous Media* (E & FN Spon, London, UK, 1997), 259.
- ²¹E. Wan and R. Van DerMerwe, "The unscented Kalman filter for nonlinear estimation," in *Adaptive Systems for Signal Processing, Communications, and Control Symposium 2000 (IEEE, Piscataway, NJ, 2000)*, pp. 153–158.
- ²²R. V. Merwe and W. Eric, "Sigma-point Kalman filters for probabilistic inference in dynamic state-space models," Ph.D. thesis, Oregon Health and Science University, 2004.
- ²³E. A. Wan and R. V. Merwe, "The unscented Kalman filter," in *Kalman Filtering and Neural Networks*, edited by S. S. Haykin (John Wiley and Sons, New York, 2001), Chap. 7, pp. 221–277.
- ²⁴J. Neisser, W. Adam, F. Beyrich, U. Leiterer, and H. Steinhagen, "Atmospheric boundary layer monitoring at the meteorological observatory Lindenberg as a part of the 'Lindenberg Column': Facilities and selected results," *Meteorol. Z.* **11**, 241–253 (2002).